Evidence for a transition in deformation mechanism in nanocrystalline pure titanium processed by high-pressure torsion

Chao Yang[a], Min Song[a], Yong Liu[a], Song Ni[a,*], Shima Sabbaghianrad[b], Terence G. Langdon[b,c]

[a] State Key Laboratory of Powder Metallurgy, Central South University, Changsha 410083, China

[b] Departments of Aerospace & Mechanical Engineering and Materials Science, University of Southern California, Los Angeles, CA 90089-1453, USA

[c] Materials Research Group, School of Engineering Sciences, University of Southampton, Southampton SO17 1BJ, UK

Abstract

Nanocrystalline titanium with an average grain size of about 60-70 nm was prepared by high-pressure torsion. The results of hardness and structural evolutions indicate that a strain induced hardening–softening–hardening–softening behavior occurs. For coarse-grained titanium, <a>-type dislocation multiplication, twinning and a high pressure induced α to ω phase transformation play major roles to accommodate deformation, leading to a significant strain hardening. As deformation proceeds, dynamic recrystallization leads to a decrease in dislocation density, especially for <a>-type dislocations, leading to a slight strain softening. The <c>-component dislocation multiplication dominates the deformation when the grain size decreases to 100 nm and <c>-component dislocation multiplication, grain refinement and the α to ω phase transformation contribute to the second strain hardening. The following stain softening is attributed to dynamic recovery.

Key words: titanium, nanostructure, deformation mechanism

*Corresponding author. Email: song.ni@csu.edu.cn (S. Ni)

Introduction

Nanocrystalline materials have drawn extensive attention over the past several decades due to their high strength, potential for superplasticity and other unique characteristics [1,2]. In practice, the deformation mechanism for nanocrystalline materials may be different from that of their coarse-grained counterparts. Thus, for face-centered cubic (FCC) materials the deformation mechanism changes from dislocation slip for coarse-grained materials to grain boundary mediated plasticity including grain boundary sliding and grain rotation for nanocrystalline materials [3-6]. Twinning may also be activated for coarse-grained FCC metals under certain circumstances but the twinning propensity decreases as the grain size decreases.

Reducing the grain size to the nanometer regime (<100 nm) can lead to the activation of deformation twinning via a new mechanism due to partial dislocation emissions from grain boundaries [4,7]. For hexagonal close-packed (HCP) materials, twinning plays an important role in the deformation mechanism of coarse-grained materials due to the insufficient number of slip systems. The twinning propensity also decreases with decreasing grain size and twinning is fully suppressed in ultrafine-grained and nanocrystalline HCP metals [8-11]. Therefore, a new deformation mechanism is needed to accommodate deformation along the c-axis for HCP materials and a possibility may be pyramidal <c+a> dislocation slip where the critical resolved shear stress (CRSS) is relatively high.

In this study, high-pressure torsion (HPT) was applied to coarse-grained pure titanium (Ti) to refine the grains from the micrometer to the nanometer range (<100 nm) and the dislocation densities

and the percentages of the <c>-component dislocations (including <c>-type dislocations and <c+a>-type dislocations) were calculated statistically at different deformation stages to elucidate their role in the deformation. The structure – hardness relationship was also examined.

Experiment

The material used in this study was commercial purity Ti cast by electric arc melting. Disks with diameters slightly less than 10 mm and thicknesses of ~1.5 mm were cut from the as-cast sample and ground down to ~0.8 mm in thickness using sand papers. The disks were then subjected to 1, 3, 5, 10 and 20 revolutions of HPT under an applied pressure of 6.0 GPa and a rotation speed of 1 rpm at room temperature using a quasi-constrained HPT facility [12] in which the change in disk thickness during HPT can be neglected. The phase compositions of both the raw material and the deformed samples were characterized using an X-ray diffractometer (XRD, Dmax 2500VB) with Cu-Kα radiation. Optical microscope (OM) observations were carried out on the surfaces of both the unprocessed material and the deformed disks after polishing using colloidal silica. Microhardness measurements were taken along radial directions of the disks at positions of 0, 1.0, 1.5, 2.0, 2.5, 3.0, 3.5 and 4.0 mm from the disk centers using a load of 50 g and a holding time of 10 s. Samples for transmission electron microscopy (TEM) were prepared by cutting disks with diameters of 3 mm from the HPT disks, mechanically grinding to ~100 μm in thickness and then electropolishing using a solution of 5% perchloric acid, 35% butanol and 60% methanol at −30 ºC with an applied voltage of 30 V. The TEM observations were conducted using a JEOL JEM-2100F microscope. The dislocation density was calculated by counting the numbers of dislocations in high-resolution TEM (HRTEM) images and dividing by the overall areas of the images.

Results

Figure 1 shows the XRD patterns of the coarse-grained (CG) material and deformed samples. It can be seen that all the peaks of the CG material can be identified to α-Ti. After 1-revolution HPT, a peak of ω titanium appears. As the number of the revolution increasing, the intensity of the ω titanium grows and more peaks of ω-Ti are observed, indicating the amount of the ω phase increases as the numbers of the revolutions increase from N=1 to N=20.

Figure 2 shows OM images of (a) the unprocessed material and (b-d) the HPT processed samples. The initial grain size was ~2 mm with a typical lamellar structure of α-Ti as shown in Fig.2(a). Figure 2(b) shows the OM image along the diameter of the 1-revolution HPT processed disk with an inserted image showing an enlarged OM image of the rectangular area. It can be seen that the lamellar structure remains at the central region of the disk but starts bending at positions having radii between 0 to 1 mm. This lamellar structure starts breaking down and forming elongated thin strips at positions with radii between 1 to 4 mm. At radii beyond 4 mm, a more even structure was obtained. As the number of HPT revolutions increased to 3, the lamellar structure in the central region became much smaller as shown in Fig.2(c). Elongated thin strips were observed in the central region with radii between 0 to 1 mm and a homogeneous structure was obtained at radii beyond 3 mm. When the numbers of HPT revolutions increased to 10 as shown in Fig.2(d), the lamellar structure disappeared even at the central region of the disk thereby indicating the development of a more homogeneous structure.

Figure 3 shows the hardness evolution as a function of the equivalent von Mises strain, ε, which is defined as $\varepsilon = \frac{2\pi Nr}{\sqrt{3}h}$, where r is the distance from the disk center, h is the thickness of the disk and N is the number of HPT revolutions [13]. As the strain increases from 0 to 15.8, the hardness increases significantly from 192 Hv to 404 Hv indicating a rapid strain hardening at the initial stage of

deformation. For the convenience of further discussion, this equivalent strain regime is defined as stage 1 (marked as S1 in Fig.3). Stain softening occurs as the equivalent strain further increases from 15.8 to 48 with the hardness decreasing to 380 Hv. This stain softening stage is defined as stage 2 (marked as S2 in Fig.3). A second strain hardening occurs with further deformation, reaching a maximum hardness value of 461 Hv at a strain value of 136. Finally, there is further strain softening and the hardness decreases to 397 Hv. The second strain hardening and softening stages are defined as stages 3 and 4 (marked as S3 and S4 in Fig.3), respectively.

Figure 4 shows typical bright field TEM images of HPT-processed samples. Figure 4(a) shows a typical microstructure observed at $r \approx 0.2$ mm in the disk processed by 1 revolution in which the corresponding equivalent strain is about 1. Microbands and dislocation cells are clearly observed. Figure 4(b) shows a typical microstructure observed at $r \approx 0.2$ mm in the disk processed for 3 revolutions with a corresponding strain of ~2.7. It can be seen that the dislocation cells evolve to dislocation-free subgrains with the boundaries clearly defined. Figure 4(c) shows a typical microstructure at $r \approx 3.5$ mm for the 1 revolution HPT disk with $\varepsilon \approx 15.8$. The area marked by dashed lines indicates that the subgrain size is significantly smaller than in (b) and the misorientation angles of the subgrain boundaries are also assumed larger than in (b) due to the larger difference in contrast. In addition to subgrains which were visible throughout the specimen, a small number of grains with sizes of ~100 nm were also observed. A similar microstructure was also observed at the edge region of the 3-revolution HPT disk but the proportion of nano-sized grains increased. Figure 4(d) shows a typical microstructure at $r \approx 3.5$ mm of the 5-revolution disk with $\varepsilon \approx 68$. Equiaxed crystals with an average grain size of ~65 nm were observed throughout the specimen. Thus, nanocrystalline Ti was obtained at a strain of about 68 which corresponds to the early stage of S3. The average grain size does not change

significantly as the strain increases further.

It should be noted that a small number of grains with sizes around or larger than 200 nm can be found in the samples at S4 with an average size of ~75 nm over the whole sample. Furthermore, no twins were observed in any of the specimens under TEM. This is consistent with a report that twinning occurs first at ambient temperature during plastic deformation of Ti but appears only when the strain is low [14]. As the strain increases, twinning ceases to operate and dislocation activities predominate thereby giving rise to the formation of microbands and dislocation cells. In the present study, no twins but microbands and dislocation cells were observed in the very initial stage of deformation. It is well known that HPT is a severe plastic deformation technique with a much higher strain applied on the disk compared with the strain induced using other processing techniques. Thus, it is proposed that twinning may not be observed even in the initial stage of HPT although the observed microbands in Fig.4(a) may develop from preformed twins [14]. Thus, the grain refinement process may be summarized as follows: (1) dislocation multiplication and twinning; (2) formation of microbands and dislocation cells; (3) subdivision of microbands into subgrains; (4) formation of randomly oriented nanograins.

In order to better elucidate the hardness evolution and to understand the hardness-structure relationship, HRTEM observations were conducted on all deformed samples. Dislocations were found in both ω-Ti and α-Ti but the dislocation density was quite low in ω-Ti compared to α-Ti. Moreover, the dislocation density in ω-Ti remained essentially unchanged as deformation proceeded. It is well known that ω-Ti is much harder than α-Ti [15] and dislocation multiplication is much more difficult in this harder phase. This is in accordance with the present HRTEM observations. Therefore, deformation-induced dislocation density evolution and the effect of dislocation density on hardness evolution were studied mainly on α-Ti in this research.

Three kinds of dislocations with different Burgers vectors were identified in α-Ti from the HRTEM images including <a>-type dislocations, <c>-type dislocations and <c+a>-type dislocations. Figure 5 shows Fourier-filtered HRTEM images taken under a zone axis of [11-20]. In Figures 5(a) and (b), Burgers circuits were drawn with Burgers vectors showing typical <a> and <c+a>-type dislocation characters. The Burgers vector in Figure 5(c) presents a component along the c-direction and it is not clear whether the dislocation is <c>-type or <c+a>-type with the <a> component parallel to the electron beam direction. Therefore, <c>-type dislocations and <c+a>-type dislocations are simply termed <c>-component dislocations throughout this report. The dislocation densities of the deformed samples were calculated statistically from a large number of HRTEM images at different deformation stages. The dislocation density of the unprocessed material was estimated from bright field images by counting the numbers of dislocation lines in the images and dividing by the total areas of the images.

The resulting data, including the dislocation density values and the percentage of the <c>-component dislocations at different deformation stages, are indicated by red triangles and blue inverted triangles in Figure 3. The dislocation density increases from 1.62×10^{12} to $4.21 \times 10^{15}\ m^{-2}$ in stage S1. The percentage of <c>-component dislocations is 32% at the end of this stage. In S2, the dislocation density drops slowly to $4.04 \times 10^{15}\ m^{-2}$ while the percentage of <c>-component dislocations rises sharply to 54% which means the percentage of <a>-type dislocations drops from 68% to 46%. In S3, the dislocation density drops to $3.26 \times 10^{15}\ m^{-2}$ initially and then increases to $5.57 \times 10^{15}\ m^{-2}$. The percentage of <c>-component dislocations also decreases initially to 34% and then rises to 52%. In S4 the dislocation density and the percentage of <c>-component dislocations drops to $3.00 \times 10^{15}\ m^{-2}$ and 30%, respectively.

Discussion

The hardness evolution as shown in Figure 3 is a consequence of the structural evolutions. In S1, the initial coarse-grained material has not been refined effectively, as shown in Figures 3(a) and (b). High densities of microbands and dislocation cells formed in this stage. In addition, the α to ω phase transformation started to occur in S1 and the amount of ω phase increased as the strain proceeded. Since the ω phase is harder than the α phase, the α to ω phase transformation as well as dislocation multiplication contribute to the strain hardening in S1. It worth mentioning that the percentage of <c>-component dislocations is only 32% while <a>-type dislocations reaches 68%. This is because the critical resolved shear stress (CRSS) for <a>-type dislocations is much lower than for <c>-type and <c+a>-type dislocations according to Schmid's law [16].

In S2, the hardness decreased a little and this is mainly attributed to the dislocation density drop during dynamic recrystallization (DRX). It is noted that, although the amount of ω phase increased and the average grain size decreased at this stage, the hardening effects induced by the α to ω phase transformation and grain refinement were overwhelmed by the effect of the decrease in dislocation density. In addition, although the overall dislocation density decreases in S2, the percentage of <c>-component dislocations increases sharply, indicating that a large number of the <a>-type dislocations disappear, while the initial <c>-component dislocations remain and probably some new <c>-component dislocations are generated. In HCP metals such as Mg, <a>-type dislocations and twin boundaries play the major role in DRX nucleation, leading to a drop in the percentage of <a>-type dislocations [17]. This is also the case for Ti in these experiments.

In S3, the hardness evolution does not follow the dislocation density evolution. The hardness increases continuously while the dislocation density experiences a decrease and a subsequent increase.

Grain refinement and the α to ω phase transformation play the major role at the beginning of the strain hardening since nanocrystalline Ti was obtained at this stage, while the effect of the dislocation density drop was compensated by grain refinement and the α to ω phase transformation. The grain size saturates thereafter and subsequent dislocation density increases and the α to ω phase transformation contribute most to the following hardness increase. In this stage, the percentage of <c>-component dislocations also experiences a sharp decrease and then a sharp increase. The sharp decrease is due to two reasons. Firstly, at the end of the DRX stage, the <c>-component dislocations join the grain boundary formation because it is only in that way that three-dimensional grains can be formed [17], thereby leading to a loss in the number of <c>-component dislocations. Secondly, although the CRSS for dislocation movement increases as the grain size decreases, the CRSS for <a>-type dislocation movement remains much lower than for <c>-component dislocations [16], so that at the beginning of the newly formed nano-grains the density of <a>-type dislocations continue to grow faster than for the <c>-component dislocations. The following increase indicates that the strain is large enough to activate the <c> component dislocation multiplication. Comparing to the first strain hardening stage S1, in which the <a>-type dislocation multiplication and α to ω phase transformation contribute most to the hardness increase, the <c>-component dislocation multiplication and the α to ω phase transformation play a major role at the second strain hardening stage (S3) in which the initial coarse-grained material in S1 has been refined to a nanocrystalline material.

The above results indicate that there are many more <c>-component dislocations participating in the deformation in nanocrystalline Ti than in coarse-grained Ti. Furthermore, twins were not observed in nanocrystalline Ti but were assumed to form in coarse-grained Ti since microbands were observed. Meyers et al. [18] reported that both twinning and dislocation movement follow the Hall-Petch (H-P)

relationship. As the grain size decreases, both twinning and dislocation movement become harder, but the slope of the twinning-grain size is larger. Okazaki and Conrad [19] reported that the H-P slope of Ti for twinning (k_t) is 3 times larger than the slope of Ti for slip (k_s). That means when the grain size is reduced to a certain number, <c>-component dislocation multiplication becomes easier than twinning and the deformation mechanism changes from twinning to <c>-component dislocation multiplication which is the case reported here. .

In S4, the dislocation density decreases with a sharp drop on the percentage of <c>-component dislocations, and some grains larger than 200 nm appears indicating the occurrence of dynamic recovery (DRV). The heat generated by HPT when processing to large revolution numbers may explain the occurrence of DRV [20]. The amount of ω phase also increased, indicating that the ω phase is stable under high pressures even when DRV occurs. But the hardening of the ω phase is not as large as the softening caused by DRV. In this stage, the percentage of <c>-component dislocations drops significantly. The <c>-component dislocations, especially <c+a> type dislocations, have a larger Burgers vector than the <a>-type dislocations which means the energy of the <c>-component dislocations is higher. In the DRV process, reducing the number of <c>-component dislocations leads to a larger energy drop and thus more <c>-component dislocations disappear in the DRV stage.

In the present investigation, when the grain size drops from the ultrafine to the nanometer region, twinning is not activated but the percentage of <c>-component dislocations rises by comparison with the coarse-grain stage. Thus, the mechanism to coordinate deformation is an increase in <c>-component dislocation multiplication instead of twinning when the grain size reaches the nanometer level in pure Ti.

Conclusions

In summary, the structural and hardness evolutions were investigated in commercial purity Ti processed by high-pressure torsion. For coarse-grained Ti, <a>-type dislocation multiplication, twinning and high pressure-induced α to ω phase transformation play major roles to accommodate deformation, leading to a significant strain hardening. Dynamic recrystallization produces a decrease in dislocation density, especially for <a>-type dislocations, leading to a slight strain softening and <c>-component dislocation multiplication dominates the deformation when the grain size is reduced to 100 nm. The <c>-component dislocation multiplication, grain refinement and α to ω phase transformation contribute to a second strain hardening and the subsequent stain softening is attributed to the advent of dynamic recovery..

Acknowledgements

Financial support from the National Natural Science Foundation of China (51301207), the China Postdoctoral Science Foundation (2013M531806), and the China Postdoctoral International Exchange Program is appreciated. This work was supported in part by the National Science Foundation of the United States under Grant No. DMR-1160966 (SS and TGL).

References

[1] Gleiter H (2000) Nanostructured materials: basic concepts and microstructure, Acta Mater. 48:1–29.

[2] Dao M, Lu L, Asaro RJ, De Hosson JTM, Ma E (2007) Toward a quantitative understanding of mechanical behavior of nanocrystalline metals. Acta Mater. 55:4041-4065.

[3]Wu X, Tao N, Hong Y, Xu B, Lu J, Lu K (2002). Microstructure and evolution of

mechanically-induced ultrafine grain in surface layer of Al-alloy subjected to USSP. Acta Mater. 50:2075-2084.

[4] Liao XZ, Zhou F, Lavernia EJ, Srinivasan SG, Baskes MI, He DW, Zhu YT (2003) Deformation mechanism in nanocrystalline Al: partial dislocation slip. Appl. Phys. Lett. 83:632-634.

[5] Liao XZ, Zhao YH, Srinivasan SG, Zhu YT, Valiev RZ, Gunderov DV (2004) Deformation twinning in nanocrystalline copper at room temperature and low strain rate. Appl. Phys. Lett. 84:592-594.

[6] Wu XL, Ma E (2006) Dislocations in nanocrystalline grains. Appl. Phys. Lett. 88 (2006) 231911 - 1 - 231911-3.

[7] Liao XZ, Zhao YH, Srinivasan SG, Zhu YT, Valiev RZ, Gunderov DV (2004) Deformation twinning in nanocrystalline copper at room temperature and low strain rate. Appl. Phys. Lett. 84:592–594.

[8]Shin DH, Kim I, Kim J, Kim YS, Semiatin SL(2003) Microstructure development during equal-channel angular pressing of titanium. Acta Mater. 51:983–996.

[9] Kim I, Kim J, Shin DH, Lee CS, Hwang SK (2003) Effects of equal channel angular pressing temperature on deformation structures of pure Ti. Mater. Sci. Eng. A 342 (2003)302–310.

[10] Kumar NVR, Blandin JJ, Desrayaud C, Montheillet F, Suery M (2003) Grain refinement in AZ91 magnesium alloy during thermomechanical processing. Mater. Sci. Eng. A 359:150–157.

[11] Wu X, Tao N, Hong Y, Liu G, Xu B, Lu J, Lu K(2004) Strain-induced grain refinement of cobalt during surface mechanical attrition treatment. Acta Mater. 53:681–691.

[12] Figueiredo R B, Cetlin PR, Langdon TG(2011)Using finite element modeling to examine the flow processes in quasi-constrained high-pressure torsion. Mater. Sci. Eng. A 528:8198-8204

[13] Zhilyaev AP, Langdon TG (2008) Using high-pressure torsion for metal processing: fundamentals and applications. Prog. Mater. Sci. 53:893-979.

[14]Zhu KY, Vassel A, Brisset F, Lu K, Lu J(2004) Nanostructure formation mechanism of alpha-titanium using smat. Acta Mater. 52:4101-4110.

[15]Todaka Y, Sasaki J, Moto T, Umemoto M (2008). Bulk submicrocrystalline ω-ti produced by high-pressure torsion straining. Scr. Mater. 59:615-618

[16] Yoo MH, Agnew SR, Morris JR, Ho KM (2001) Non-basal slip systems in hcp metals and alloys: source mechanisms. Mater. Sci. Eng. A, 319:87-92.

[17]Galiyev A, Kaibyshev R, Gottstein G (2001) Correlation of plastic deformation and dynamic recrystallization in magnesium alloy ZK60. Acta Mater. 49:1199-1207.

[18] Meyers MA, Vöhringer O, Lubarda VA (2001) The onset of twinning in metals: a constitutive description. Acta Mater. 49:4025-4039.

[19] Okazaki K, Conrad H (1973) Effects of interstitial content and grain size on the strength of titanium at low temperatures. Acta Metal. 21:1117-1129.

[20] Pereira PHR, Figueiredo RB, Huang Y, Cetlin PR, Langdon TG (2014) Modeling the temperature rise in high-pressure torsion. Mater. Sci. Eng. A, 593:185-188.

Figure captions:

Figure 1: XRD patterns of the coarse-grained material and deformed samples (colored online).

Figure 2: The OM images of (a) the coarse-grained material, (b) the OM image along the diameter of the 1-revolution HPT-processed disk, (c) the OM image along the diameter of the 3-revolution HPT-processed disk and (d) the OM image at the center of the 10-revolution HPT-processed disk.

Figure 3: Relationship between strain and microhardness, dislocation density and percentage of <c>-component dislocations of HPT samples (colored online).

Figure 4: Bright field TEM images of (a) the center region of the 1-revolution HPT-processed disk, (b) the center region of the 3-revolution HPT-processed disk, (c) the edge region of the 1-revolution HPT-processed disk, (d) the edge region of the 5-revolution HPT-processed disk.

Figure 5: Fourier-filtered HRTEM images of deformed specimens taken under zone axis of [11-20]. Burgers circuits for <a>-type dislocation and <c+a>-type dislocation were drawn in (a) and (b), respectively. Burgers circuit with a Burgers vector presenting a component along the c direction was drawn in (c) which may be a <c>-type or <c+a>-type dislocation.

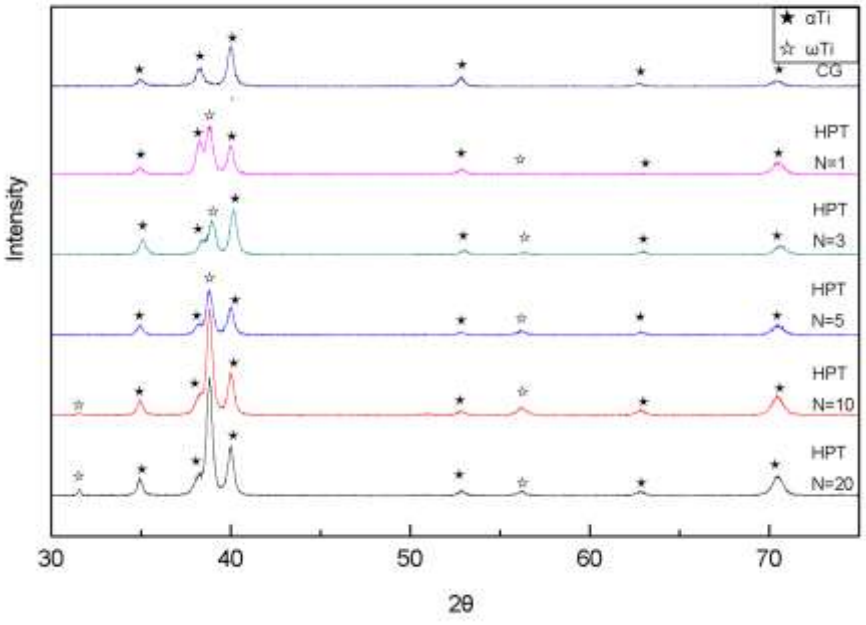
★ αTi
☆ ωTi
CG
HPT
N=1
HPT
N=3
HPT
N=5
HPT
N=10
HPT
N=20
Intensity
30
40
50
60
70
2θ

Fig. 1

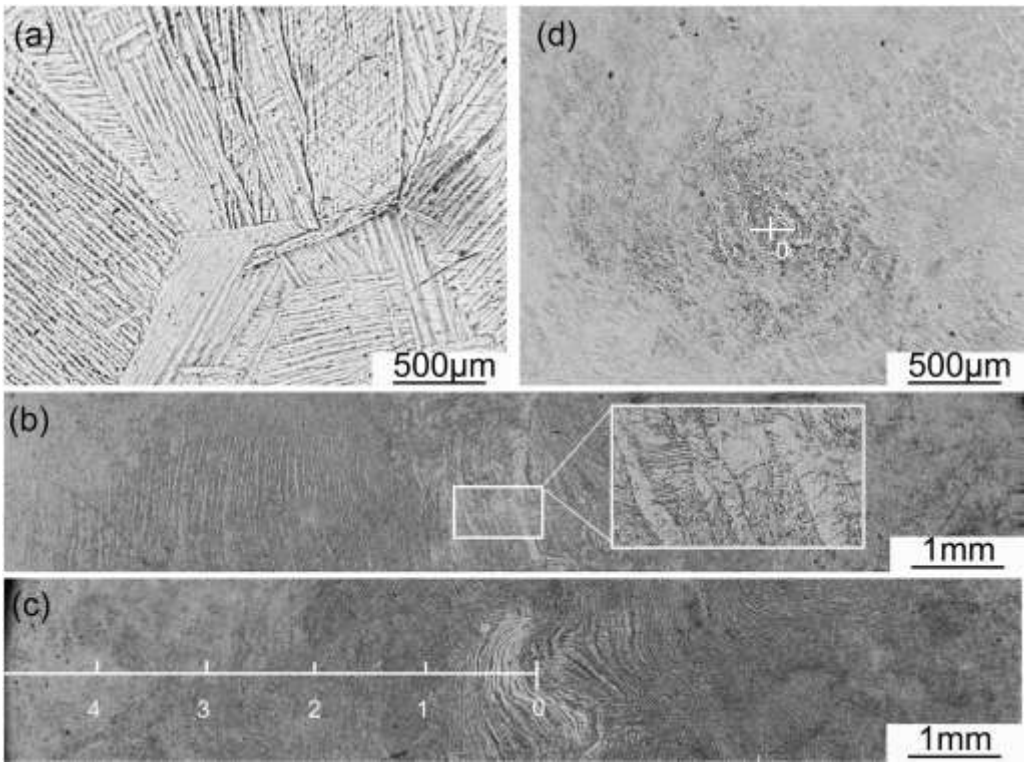

Fig. 2

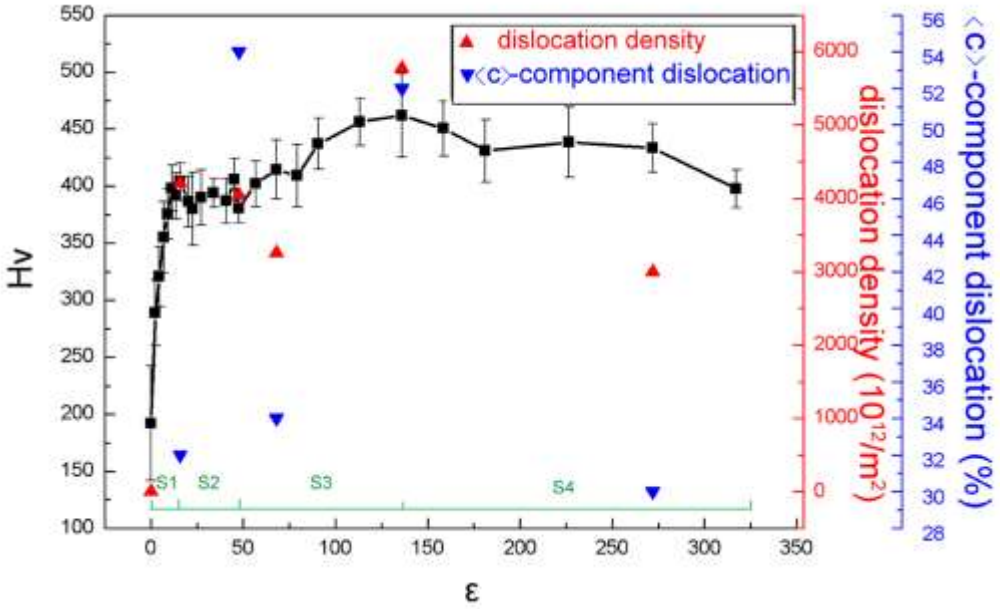
dislocation density
<c>-component dislocation
Hv
dislocation density (10^12/m^2)
<c>-component dislocation (%)
ε
S1
S2
S3
S4

Fig. 3

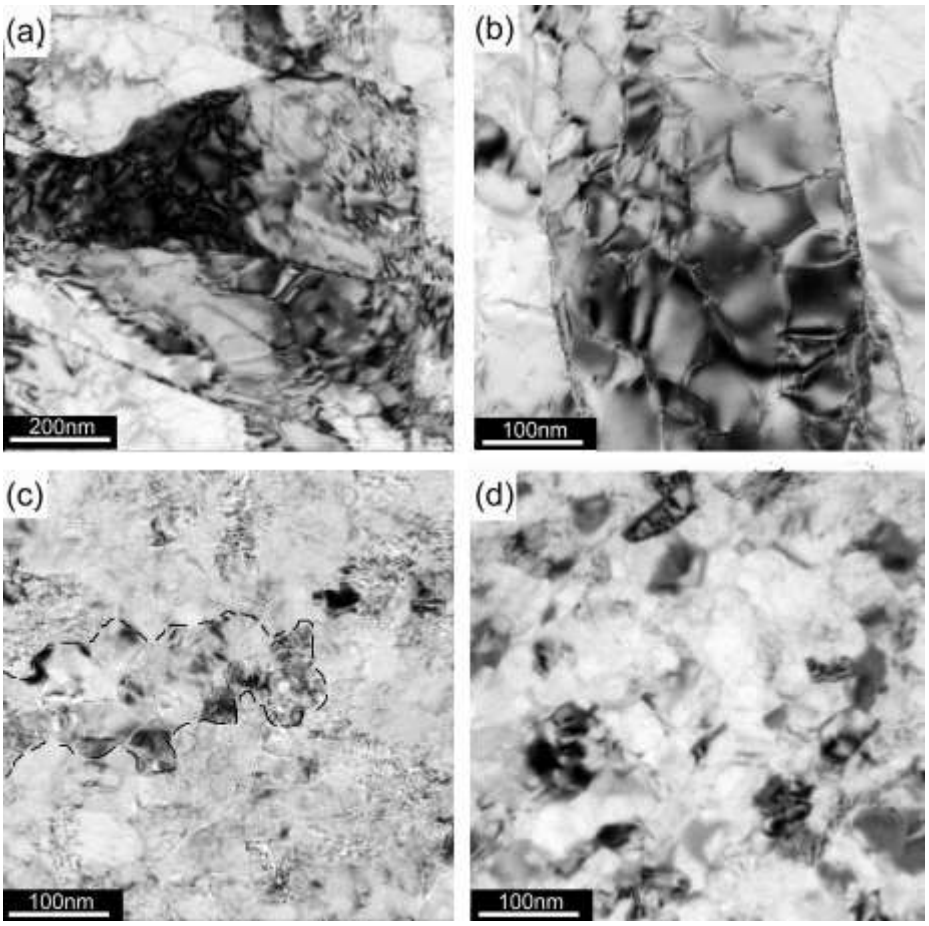

Fig. 4

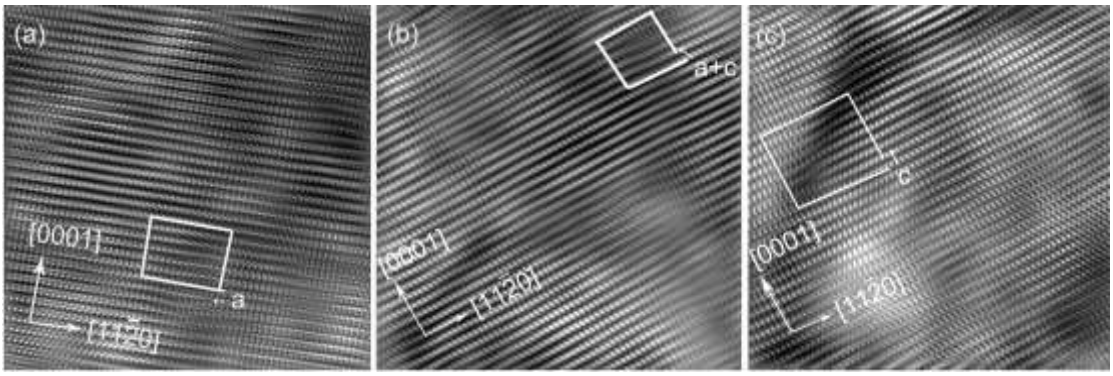

Fig. 5